Lab on a Chip

PAPER

View Article Online
View Journal | View Issue

Cite this: *Lab Chip*, 2021, **21**, 4208

Bacterial classification and antibiotic susceptibility testing on an integrated microfluidic platform†

Alexandros A. Sklavounos, ‡[ab] Carine R. Nemr,‡[a] Shana O. Kelley [acd] and Aaron R. Wheeler *[abd]

With the prevalence of bacterial infections and increasing levels of antibiotic resistance comes the need for rapid and accurate methods for bacterial classification (BC) and antibiotic susceptibility testing (AST). Here we demonstrate the use of the fluid handling technique digital microfluidics (DMF) for automated and simultaneous BC and AST using growth metabolic markers. Custom instrumentation was developed for this application including an integrated heating module and a machine-learning-enabled low-cost colour camera for real-time absorbance and fluorescent sample monitoring on multipurpose devices. Antibiotic dilutions along with sample handling, mixing and incubation at 37 °C were all pre-programmed and processed automatically. By monitoring the metabolism of resazurin, resorufin beta-D-glucuronide and resorufin beta-D-galactopyranoside to resorufin, BC and AST were achieved in under 18 h. AST was validated in two uropathogenic *E. coli* strains with antibiotics ciprofloxacin and nitrofurantoin. BC was performed independently and simultaneously with ciprofloxacin AST for *E. coli*, *K. pneumoniae*, *P. mirabilis* and *S. aureus*. Finally, a proof-of-concept multiplexed system for breakpoint testing of two antibiotics, as well as *E. coli* and coliform classification was investigated with a multidrug-resistant *E. coli* strain. All bacteria were correctly identified, while AST and breakpoint test results were in essential and category agreement with reference methods. These results show the versatility and accuracy of this all-in-one microfluidic system for analysis of bacterial growth and phenotype.

Received 10th July 2021,
Accepted 15th September 2021

DOI: 10.1039/d1lc00609f

rsc.li/loc

Introduction

The use of antibiotics to treat bacterial infections is becoming ever more challenging as the prevalence of antibiotic resistance increases. The main contributor to this issue is the excessive and inappropriate use of antibiotics, which has led to drug resistance *via* many different mechanisms in various strains of bacteria.[1,2] Antibiotic susceptibility testing (AST) is performed to determine the minimum inhibitory concentration (MIC) of antibiotics, which identifies the likelihood of a particular drug's therapeutic success against a given infection.[3] In many applications, it is also useful to conduct bacterial classification (BC) studies (*e.g.*, to indicate whether the sample contains coliform bacteria or not) as additional data to inform therapeutic decision-making (note the difference between the 'classification' methods described here and the more involved level of testing required to precisely 'identify' bacterial species, which rely on complex amplification or sequencing schemes[4–7] and/or mass spectrometry[8]). AST and BC results can take up to 48 h or more to collect, which can lead to delays in prescribing appropriate antibiotics or to the administration of inappropriate antibiotics prior to obtaining AST results, affecting morbidity, mortality, severity of infections and the prevalence of antibiotic resistance.[9]

BC and AST are broadly applicable in various sectors, being routinely performed in healthcare diagnostics, food safety and water quality testing.[10] In the healthcare industry, urinary tract infections (UTIs) are among the most widespread community and hospital-acquired bacterial infections and are the second most common infections to be prescribed antibiotics.[11] UTIs are primarily caused by uropathogenic *E. coli*, which have developed resistance to common antibiotics used to treat UTIs (*e.g.*, ciprofloxacin, nitrofurantoin, ampicillin, *etc.*) with varied prevalence in different regions of the world.[11,12] The mechanisms of resistance to these drugs of different antibiotic classes are diverse and novel types of resistance may arise in the future, posing challenges for molecular diagnostic testing. In food and water quality testing, BC allows classifying coliform bacteria to detect sanitary contamination.[13,14]

[a] *Department of Chemistry, University of Toronto, 80 St. George Street, Toronto, Canada. E-mail: aaron.wheeler@utoronto.ca*
[b] *Donnelly Centre for Cellular and Biomolecular Research, University of Toronto, 160 College Street, Toronto, Ontario, M5S 3G9, Canada*
[c] *Department of Pharmaceutical Science, University of Toronto, 144 College Street, Toronto, Ontario, M5S 3E5, Canada*
[d] *Institute of Biomedical Engineering, University of Toronto, 164 College Street, Toronto, Ontario, M5S 3G9, Canada*
† Electronic supplementary information (ESI) available. See DOI: 10.1039/d1lc00609f
‡ These authors contributed equally.

Standard AST performed in clinical settings includes agar dilution, broth microdilution, disk diffusion and commercial assays such as the bioMérieux Etest.[15] Though cost-effective, these tests lack automation, require long culture times and do not provide BC information (requiring additional tests). Furthermore, conventional methods require well-trained personnel to ensure successful completion of tests under aseptic conditions. A few automated systems that typically measure turbidity, fluorescence or colorimetric changes for AST (some with integrated BC) have been approved by the Food and Drug Administration.[15,16] These instruments are powerful and useful, but are generally bulky and costly, which is prohibitive for low resource settings, while their proprietary interfaces and test formats do not allow the design of custom protocols.

Over the last 15 years, microfluidics, an established technology that permits the manipulation of small volumes of fluids, has gained traction for application to AST and BC.[17,18] Using micrometre-sized fluidic channels, these devices allow for rapid, high-throughput and low-cost analyses.[19–35] With these advantages come certain caveats; microfluidic systems often lack full integration and facile on-the-spot customizability. For example, the majority of microfluidic devices require external flow systems, such as pumps, to manipulate liquids.[26,27,30,34,35] Despite the fact that the microfluidic chips are simple and inexpensive, incubators are still needed for device operation when culture is required.[28,32] Moreover, fast detection capabilities for these systems often rely on large, ancillary equipment such as microscopes,[19,21,31] making the techniques ill-suited for operation in near-patient settings. Finally, above all, changes in analytical protocols typically require the complex task of redesigning devices.[29]

An alternative microfluidic technology, dubbed digital microfluidics (DMF), enables on-demand manipulation of individual, low-volume droplets on an array of electrodes, using electrostatic forces. Unlike traditional microfluidics, DMF eliminates the need for pumps or other external mechanical actuators and is resistant to clogging due to the open nature of the device.[36] As shown previously, the surfaces of DMF devices are biocompatible and do not inhibit cell growth,[37] making DMF an ideal platform for bacterial culture.[38] Recently, the first DMF method was reported for carrying out phenotypic AST.[39] The methods described therein feature embedded oxygen sensors, and the results suggest great potential for a DMF approach to this application. But the system that was used was relatively bulky, relying on external optics for beam steering and detection and a large, homemade incubator, and was reported to be useful for AST only, without BC. Here, we report a new system that addresses these limitations.

The system described here is a fully integrated, user-friendly DMF instrument, designed to perform customizable phenotypic AST and BC protocols. The instrumentation includes an integrated heating module and a low-cost colour camera to achieve multipurpose absorbance and fluorescence measurements. Protocol steps, including on-device antibiotic dilutions, sample handing and mixing, as well as incubation at 37 °C, were all automated with an intuitive user interface. Methods were developed and results presented for automated DMF AST, breakpoint testing, and BC, implemented both as stand-alone assays and in parallel configurations. We propose that this all-in-one microfluidic system for analysis of bacterial growth and phenotype represents a useful addition to the genre, potentially serving as a prototype for a commercial system that could operate in settings both inside or outside of the laboratory.

Materials and methods

Reagents and materials

Mueller Hinton broth (MHB), *E. coli* (EC) broth, nitrofurantoin, resazurin sodium salt, resorufin beta-D-glucuronide (REG) sodium salt, resorufin beta-D-galactopyranoside (RGP), *N*,*N*-dimethylformamide, GFDX103000 glass fibre diagnostic pads and MicroAmp optical adhesive film were purchased from Millipore Sigma, MO. Ciprofloxacin hydrochloride monohydrate was obtained from Thermo Fisher Scientific, MA. Ethylenediamine tetrakis(ethoxylate-block-propoxylate) tetrol (Tetronic 90R4) was obtained from BASF, Germany. Vapor-lock was supplied by Qiagen Hilden, Germany. Unless otherwise specified, electronic components were purchased from Digi-Key, MN.

DMF device fabrication

DMF glass bottom plates (76.2 mm × 76.2 mm × 1.1 mm) bearing chromium electrodes, coated with parylene C and FluoroPel PFC 1104 V (Cytonix LLC), were fabricated in the University of Toronto Nanofabrication Centre cleanroom facility, as previously described.[40] The bottom plate design featured an array of 78 cross-shaped actuation electrodes, 6 rectangular mixing electrodes, 6 square electrodes, 10 rectangular dispensing electrodes, and 10 reservoir electrodes (Fig. S1†). Each electrode was connected *via* a patterned wire that interfaced with an array of electrode pads on the side of the device. DMF top plates consisted of indium tin oxide-glass slides (25.4 mm × 50.8 mm × 0.7 mm, Riley Supplies) coated with FluoroPel PFC 1104 V, as described previously.[41] 9876-15 copper tape (3M, MN) was wrapped around the edge of the bottom plate of the DMF device to serve as ground connection to the top-plate. Each device was assembled by joining the top and bottom plate with two layers of Scotch double-sided tape (3M, MN), which served as a spacer creating an inter-plate gap of approximately 200 μm and holding the two parts of the device together. J-B Weld plastic bonder (Canadian Tire, Canada) was used to bind the two plates together. Unit droplets (*i.e.*, those that covered a single actuation electrode) were approximately 1.1 μL, and reservoir volumes (*i.e.*, droplets that covered a single reservoir electrode) were approximately 7.5 μL.

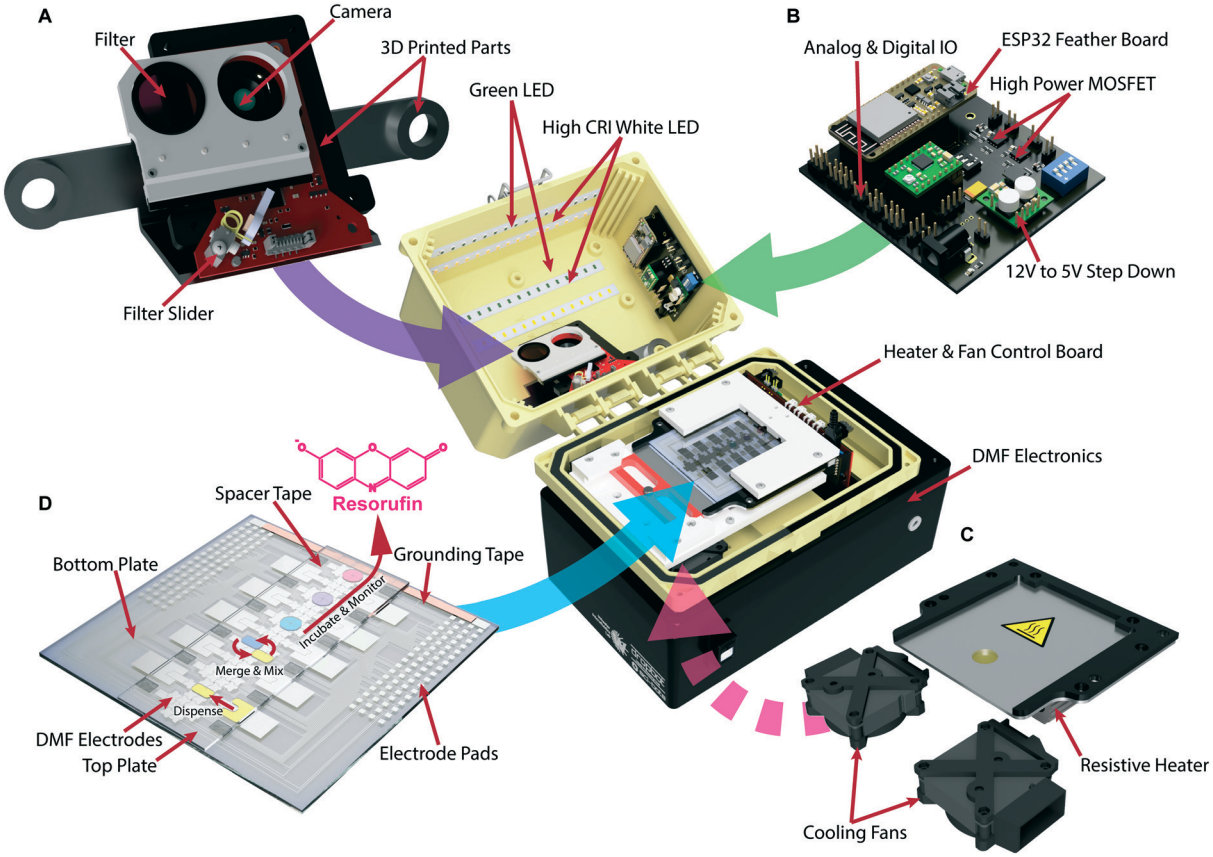

Fig. 1 Rendered image of the DMF instrument (25 cm × 19 cm × 23 cm). (A) Camera and filter changer, mounted on a 3D printed base, for absorbance and fluorescence image acquisition of the DMF device. (B) GPIO board for filter slider and light control. (C) Heating unit containing a resistive heater and a set of cooling fans. (D) DMF device made up of a bottom plate (76.2 mm × 76.2 mm) with electrodes, electrode pads and grounding tape. A top plate is connected to the bottom plate *via* spacer tape (~200 μm). Solutions are dispensed in unit-droplet volumes (each unit is 1.1 μL) on the device and can be merged/mixed and incubated for real-time monitoring of resorufin production to detect bacterial metabolic activity.

DMF instrumentation

The DMF instrument used here (Fig. 1) was a modified, customized version of a predecessor that is described in detail elsewhere.[42] The outer dimensions were 25 cm × 19 cm × 23 cm ($w \times l \times h$) and the box weighed ~3.9 kg. The DMF control boards and pogo-pin board were purchased from Sci-Bots Inc. (Kitchener, ON) and were adapted from DropBot V3 (Sci-Bots Inc.). The boards were connected using a custom printed circuit board (PCB) that included power electronics, slots for the DMF control boards and pogo-pin board, as well as custom power outlets for 12 V and 3 V that powered external devices.

As described elsewhere,[42] the base of the instrument included a heating unit and a set of cooling fans (4010, WINSINN, Amazon.ca). The heating unit (Fig. S2†) comprised an aluminium plate (108 mm × 95 mm × 1.65 mm, McMaster-Carr) on which two chassis-mount resistors (10 Ω, THS5010RJ, TE Connectivity) were attached 66 mm apart. A thermistor strip, containing three negative temperature coefficient thermistors (10 kΩ, NTCG103JX103DTDS, TDK Corporation), was placed between the two resistors to monitor the temperature of the aluminium plate. A polyimide (Kapton®) film coated with copper was patterned in-house to serve as wiring for the thermistors. Another layer of polyimide (Kapton®) film tape was placed atop the thermistors to protect them from wear. The maximum allowable temperature of the bottom heating unit was 100 °C.

New for this work, the lid of the instrument was equipped with an ELP-USB8MP02G-L28 camera (Ailipu Technology Co., Ltd, China) with 0.5 lux minimum illumination sensitivity and an ELL6 dual-position filter slider (Thorlabs, NJ) mounted on a 3D printed arm (polylactic acid, printed with Ultimaker 2). An FB600-40 bandpass filter (Thorlabs, NJ) with centre wavelength (CW) 600 ± 8 nm and full width at half max (FWHM) 40 ± 8 nm was mounted on the left filter position of the ELL6 filter slider for fluorescence measurements; the right filter position was left open for absorbance measurements. Four high colour rendering index (CRI) white light emitting diode (LED) strips (Marswalled, Amazon.ca) and four green LED strips (XT Auto, Amazon.ca) were affixed on the inside of the instrument lid for absorbance and fluorescence measurements, respectively. The filter slider and lights were controlled by a custom

general-purpose input–output (GPIO) board that was also placed next to the LEDs.

DMF device control

Devices were managed using a custom version of the open-source DropBot system[43] (version 3.0, https://github.com/sci-bots/dropbot-v3) that included a peripheral board allowing the control of heating elements, as described elsewhere.[42] The DropBot and heater unit were controlled using a custom version of MicroDrop software (version 2.31.1, https://github.com/sci-bots/microdrop). Devices were interfaced to the DropBot and were actuated in pre-programmed steps to facilitate droplet dispensing, moving, and mixing by applying 100 V_{RMS} square waves at 10 kHz. These parameters generate forces below the velocity-saturation for the liquids used in this work, as determined experimentally (Fig. S3†) using a method described previously,[44] with the improvement that the applied force (horizontal error bars) was calculated from the measured applied voltage at each step.

Filter and light control on DMF

A custom GPIO PCB (Fig. S4†) operated by an ESP32 Feather Board (Adafruit Industries, NY) was used to control the filter slider and the LEDs. The board included two high-power transistors (SQJA60EP-T1_GE3, Vishay Siliconix) to control the state and intensity of each LED strip (white and green). The filter slider was controlled over serial communication. The board was powered with 12 V from DropBot and a 12 V to 5 V step down (D24V25F5, Pololu, NV) was used to power the ESP32 board with 5 V.

Custom firmware was developed in C++ to allow the board to communicate with and be controlled by the host computer over Bluetooth. The firmware included a set of instructions to control the state and power of LEDs, as well as initialize, calibrate, and use the filter slider. A user interface (UI) was developed in Python using PyQt5[45] and OpenCV[46] libraries (Fig. S5†) for remote control of the GPIO board (LEDs and filter slider position), annotating the droplets on the device with sample labels and capturing images from the USB camera at set intervals. The UI also included bundled controls for fluorescence mode (turn on green LEDs, move slider to filter position and set camera exposure time to 640 ms), absorbance mode (turn on white LEDs, move slider to no filter position and set camera exposure time to 2.5 ms) and dual mode (absorbance mode followed by fluorescence mode).

Image acquisition and pre-processing

Images were captured on the on-board camera operating at its maximum resolution (3264 × 2448 pixels) and processed using a custom script written in Python 3. The camera's distortion was determined by capturing test images of a chess board pattern (7 × 10) captured at different locations and orientations. The test images were used to calculate a 3 × 3 camera matrix, which contained the intrinsic parameters of the camera [focal length (f_x, f_y) and optical centres (c_x, c_y)], as well as the distortion coefficients (radial distortion coefficients, k_n and tangential distortion coefficients, p_n).

Custom camera matrix for distortion correction including the focal length (f_x, f_y) and optical centres (c_x, c_y) of the camera:

$$\begin{bmatrix} f_x & 0 & c_x \\ 0 & f_y & c_y \\ 0 & 0 & 1 \end{bmatrix} = \begin{bmatrix} 2353.2 & 0 & 1569.6 \\ 0 & 2365.5 & 1185.8 \\ 0 & 0 & 1 \end{bmatrix} \quad (1)$$

Radial distortion coefficients k_n and tangential distortion coefficients p_n of the camera:

$$[k_1 \ k_2 \ p_1 \ p_2 \ k_3] = [-0.3951 \ \ 0.2087 \ \ 0.0032 - 0.0002 \ \ -0.0685] \quad (2)$$

Image pre-processing was carried out in seven steps, as outlined in Fig. S6.†

1. Raw red, green, blue (RGB) images (3264 × 2448 pixels) were captured from the camera (Fig. S7†) and stored locally.

2. Images captured without a filter (absorbance mode, Fig. S7A†) were not colour-corrected. Images captured with a filter (fluorescence mode, Fig. S7B†) were colour-corrected as follows. The images were split into the individual channels (R, G and B). The green (G) channel was added to the red (R) to correct for known effect of light entering the filter at angles higher than 30° being incorrectly recorded as green.[47] The channels (including R + G as R, G, and B) were then recombined to form corrected RGB fluorescence images.

3. Raw images were undistorted using the precalculated camera matrix (eqn (1)) and distortion coefficients (eqn (2)).

4. The undistorted images were corrected for perspective as described previously.[48] Briefly, four coordinates in the source image and four reference coordinates were defined. A 3 × 3 matrix was calculated based on each set of coordinates (image – reference corresponding pair) and then the same matrix was used to transform the source image into the perspective-corrected image.

5. The luminosity profile of each image was normalized. First, the colour space of the image was converted from RGB to LAB, where the L channel represents the luminosity of the image. Then the maximum pixel intensity of each column and each row of the L channel was extracted and stored in 1D arrays. Each 1D array was then multiplied by a unit matrix with the same shape as the image to generate two 2D arrays (max-col and max-row) representing the maximum column and row pixel intensities, respectively. The max-col and max-row images were then blurred using a kernel that was five times smaller than the smallest image dimension [min(width, height)/5] and then the pixels in the max-col and max-row images were averaged to generate the luminosity profile of the image. Finally, the luminosity profile was subtracted from the L channel of the image, and the colour space of the corrected image was reverted to RGB.

6. A zero matrix (pixel values = 0) with the same shape as the corrected image was constructed and the device design was drawn on it (pixel values = 255) to create a mask of the

device electrodes (excluding the reservoir electrodes). One of the middle electrodes from the device design was used to align the luminosity-corrected image to the mask. The same mask was then used to locate the device electrodes and to define regions of interest (ROIs).

7. Using the locations of the ROIs the aligned image was split into separate square images (361 × 361 pixels) and each was resized to 256 × 256 pixels. The resized images acquired in absorbance mode served as inputs for the convolutional neural network (CNN), which was used to identify the contour of the droplets on the DMF device.

Convolutional neural network for droplet localization/detection

A CNN was built and trained to identify the outline of the droplets on the DMF chip. The network had an architecture similar to the previously reported U-Net[49] and is represented in Fig. S8.† Briefly, the input of the network was a square three channel image (channels R, G and B) with dimensions of 256 × 256 pixels. A contracting path was applied, comprising the repeated application of two convolutions using a 3 × 3 kernel, each followed by an exponential linear unit (ELU) and a max pooling operation using a 2 × 2 kernel with a stride equal to the width of the kernel (stride = 2) for down-sampling. After each down-sampling step, the number of feature channels was doubled. An expanding path was then applied, comprising an initial up-sampling operation using a 2 × 2 kernel ("up-convolution"), which halved the number of feature channels. The up-sampled feature map was then concatenated with the correspondingly cropped feature map from the contracting path and was convoluted twice using a 3 × 3 kernel, each followed by an ELU. The final layer was a 1 × 1 convolution used to map each 4-component feature vector to the desired number of classes. The network had a total of 42 layers.

A set of 55 images of DMF devices collected under absorbance mode at various time steps of the AST (marker = resazurin) and BC experiments (marker = resazurin, RGP or REG) containing nine four-unit sample droplets (with and without bacteria) was defined as the training set. An analogous set of 15 images collected under the same conditions was defined as the validation set. Each image (after passing through the 7-step pre-processing regimen, above) contained nine ROIs, resulting in a total of 495 square training images and 135 validation images. The training set was then augmented using random brightness and blur variations to teach the network the desired invariance and robustness properties. Drop-out layers between the two convolutions of each of the steps of the contracting path were included for further data augmentation. A batch size of a single image was used to minimize the overhead and to allow maximum use of the graphics processing unit memory. Using the Adam optimizer[50] at a learning rate of 0.0001 and combining the final feature map with the cross entropy loss function, the validated model reached 0.988 accuracy and 0.0289 loss after 33 epochs (Fig. S9†).

Macro-scale bacterial culture

Two strains of *E. coli* were used for AST experiments: multidrug-resistant *New Delhi metallo-beta-lactamase (NDM-1)*-positive strain 1001728[12] (ATCC® BAA-2469™, isolated from human urine), and uropathogenic strain CFT073[51] (ATCC® 700928™, isolated from human urine and blood). *E. coli* (strain CFT073), *Klebsiella pneumoniae* (ATCC® 700603™), *Proteus mirabilis* (ATCC® 29906™) and *Staphylococcus aureus* (ATCC® 29213™) were employed in BC experiments. All 6 strains were studied in simultaneous BC and AST experiments. *E. coli* (strain 1001728) was employed for simultaneous breakpoint testing and BC. All bacterial strains were cultured in MHB overnight at 37 °C with shaking at 250 RPM. Bacterial suspensions were adjusted to desired densities by optical density measurements at 600 nm (OD_{600}) using a Spectra Max M2 microplate reader (Molecular Devices, LLC) and dilution in specified broths. Methods for standard AST tests and comparison of resorufin fluorescence to bacterial titer in a well-plate format are described in the ESI† file.

Experimental setup on DMF

DMF devices were subjected to UV irradiation for sterilization prior to solution dispensing. All solutions dispensed on DMF devices contained 0.1% wt/wt Tetronic 90R4 to allow droplet movement. Droplets were diluted, mixed, split and combined on the device. Loading reagents into reservoirs was achieved in two steps. First, a 0.5 μL aliquot of vapor-lock was deposited onto the edge of the designated reservoir. Second, a 5 μL aliquot of the reagent was deposited onto the vapor-lock, which spontaneously formed a thin 'shell' around the aqueous reagent. Upon actuation of the reservoir electrode, the two-phase volume wicked between the two plates, with the aqueous droplet centred within the vapor-lock shell. In subsequent dispensing steps, the dispensed daughter droplets were observed to maintain a vapor-lock shell, as well.

Each AST experiment began with the automated formation of a 2-fold dilution series of antibiotic solutions using a method similar to one described previously[52] in five steps (Fig. S10†). Briefly, (i) a pre-designated number of two-unit droplets (2.2 μL) of diluent (MHB with 0.25 mM resazurin) were dispensed from the reservoir electrodes and stored temporarily on the actuation electrode array. The number of diluent droplets dispensed in this step was equal to the number of on-chip dilutions being performed, plus an additional droplet to serve as the growth control (GC). A four-unit droplet (4.4 μL) of diluent was also dispensed to serve as a sterility control (SC). (ii) Two two-unit droplets of a solution containing a known amount of an antibiotic in diluent were dispensed from a reservoir electrode. One was stored temporarily on the actuation electrode array (serving as the droplet of highest antibiotic concentration in the dilution series) and the other served as the first "concentrated working droplet" (CWD) to form the dilution series. (iii) The CWD was merged with an adjacent diluent droplet to form a

four-unit droplet that was mixed for 1 min in a rectangular pattern involving 4 actuation electrodes and a mixing electrode. (iv) Upon mixing, the four-unit droplet was split into two equal two-unit droplets. (v) One two-unit droplet was stored temporarily on the chip (serving as a member of the dilution series) while the other two-unit droplet was used as the next CWD for further dilution similarly to step ii. Steps iii to v were repeated to generate the desired number of antibiotic dilutions on the DMF device; when step v was reached for the final dilution, one of the two two-unit droplets was stored on the device (serving as the droplet with lowest concentration of antibiotic in the dilution series), while the other two-unit droplet was discarded.

In standard AST experiments, the automated method above was used to generate a seven-step dilution series of antibiotic at different concentrations (seven two-unit droplets), a GC (a two-unit droplet) and an SC (a four-unit droplet). Eight two-unit diluent droplets containing 10^6 CFU mL^{-1} bacteria were then dispensed onto the array, where each droplet was merged with one of the dilution series droplets or the GC. The eight four-unit droplets were then mixed by moving in a rectangular pattern involving 6 actuation electrodes for 1 min. The final bacterial density was thus 5×10^5 CFU mL^{-1} in each droplet, matching the density used in standard broth microdilution assays.[53] Finally, the nine four-unit droplets were positioned in a line for incubation and analysis as shown in Fig. S7,† with the SC on the left and GC on the right.

In BC experiments, a truncated procedure (without antibiotic or a dilution series) was used. First, nine two-unit droplets of EC broth containing one of the three indicators (three droplets each with 0.5 mM resazurin, 0.5 mM REG or 1 mM RGP) were dispensed onto the array. Next, six two-unit droplets of 10^6 CFU mL^{-1} bacteria in EC broth (three droplets per strain – thus, each experiment evaluated two different strains) plus an additional three two-unit droplets of EC broth alone (for SCs) were dispensed onto the array, and each was merged and mixed with one of the indicator droplets. The four-unit droplets were mixed and positioned as described for AST experiments.

In experiments involving simultaneous AST and BC, similar procedures as described above were followed. Seven droplets (in MHB) and two droplets (in EC broth) were employed for AST and BC, respectively. Automated dilutions of the antibiotic ciprofloxacin were performed for AST with five final concentrations spanning susceptible, intermediate and resistance antibiotic ranges for *Enterobacteriaceae*, as per the Clinical and Laboratory Standards Institute (CLSI) AST criteria.[54] GC and SC droplets were also dispensed for AST. One test droplet and one SC droplet were dispensed for BC, where REG was used as an indicator.

In simultaneous breakpoint testing and BC experiments, automated antibiotic dilutions were performed for two antibiotics (nitrofurantoin and ciprofloxacin in MHB) for two final concentrations of each antibiotic at intermediate and susceptible values for *Enterobacteriaceae*, as per the CLSI criteria.[54] GC and SC droplets (in MHB) were also dispensed for AST. REG and RGP indicators were used for *E. coli* and coliform classification (in EC broth), respectively. A 1 : 1 mixture of REG and RGP was used as the BC SC.

In all experiments, the temperature of the device was set to and maintained at 37 °C, and humidity levels were maintained by filling otherwise unused reservoirs with distilled water, sealing the device sides with MicroAmp film, and placing stacks of GFDX103000 glass fibre diagnostic pads saturated with water atop the top plate (in regions that did not interfere with imaging). The final array of droplets was held stationary and incubated for at least 16 h, with images collected in absorbance and/or fluorescence mode (with camera and LED settings indicated above) in 5 or 10 min intervals.

DMF image analysis

For AST experiments, stacks of time-stamped ROI images collected in both absorbance mode and fluorescence mode were pre-processed as described above for each droplet being evaluated. Time-stamped ROI stacks for each sample condition (droplets containing antibiotic) were accompanied by time-stamped ROI image stacks for a GC and an SC. For each condition evaluated (sample, GC, and SC), the output of the trained CNN was used to identify the droplet contours of each absorbance-mode image to form a time-stamped mask, which was then applied to each corresponding absorbance-mode and fluorescence-mode ROI image to isolate the pixels within each droplet.

1. The number of unmasked pixels in each ROI was recorded and converted into a 1D array with respect to time as a measure of droplet area. The array was then normalized by dividing each value by the maximum value in the array.

2. For each stack of fluorescent ROI images, the mean and standard deviation of the pixel values in the unmasked region of each image was recorded as signal S and σ, respectively, which were then converted into 1D arrays of S and σ with respect to time for that condition.

3. The median of the values for the first ten timepoints in each signal array was calculated and subtracted from the series as a first baseline correction.

4. The baseline-corrected signal array and the standard deviation array were multiplied by the array of relative droplet areas to correct for evaporative loss.

5. The minimum signal S_{min} was determined for each signal array and was subtracted from all values as a second baseline correction.

6. The maximum signal S_{max} was determined for each signal array (including sample, GC,[55] and SC). For signal arrays in which $S_{max} \geq S_{max,GC}$, the array was normalized by dividing all values by S_{max}. For arrays in which $S_{max} < S_{max,GC}$, the array was normalized by dividing all values by $[S_{max,GC} + 3 \times \sigma_{S_{max,GC}}]$. At the end of step 7, all signal arrays contained normalized signals S_N in the range [0, 1].

7. The time required for each signal in each sample containing growing bacteria to reach the first mid-point of

the curve t_M was recorded as a marker of bacterial viability. Specifically, in each signal array, the first timestamp with $S_N > 0.5$ was recorded as t_+ and the timestamp immediately preceding that point was recorded as t_-. A linear fit between the signals at t_+ and t_- was then applied to determine the intermediate t_M at which S_N was predicted to be 0.5. For conditions that did not yield growing bacteria (*e.g.*, the SC or other conditions with low signals that never reached S_N = 0.5), t_M was defined as 18 h.

8. A percent viability value was determined for each experimental condition from eqn (3), and the MIC for each antibiotic was then calculated from this value as described for the broth-microdilution technique.

Percent viability calculation in DMF experiments from growth curve measurements, where $t_{M,SC}$, $t_{M,sample}$, and $t_{M,GC}$, were the times required to reach mid-point of the growth curve for the SC, the sample being evaluated, and the GC, respectively:

$$\%\ \text{viability} = 100\% \times \frac{t_{M,SC} - t_{M,sample}}{t_{M,SC} - t_{M,GC}} \quad (3)$$

BC experiments evaluated replicate droplets of bacteria exposed to three different indicators. Stacks of time-stamped ROI images were evaluated using a modified/truncated version of the procedure indicated above, in which steps 1–5 were identical, and in step 6, 1D signal arrays with respect to time were tested with the peak finding algorithm from the SciPy package[56] – those bearing a peak (with minimum distance in between peaks = 20 points, peak width between 5 and 30 points and "peak prominence" = 2) were designated as "positive", while others were designated as "negative".

For both AST and BC experiments, the steps listed above were applied to the R, G, and B channels of both absorbance-mode and fluorescence-mode images, but in these analyses only the R channel signal under fluorescence-mode was used as the assay signal.

Results and discussion

A DMF platform for integrated bacterial culture and analysis

Motivated by the growing problem of antibiotic resistance, we developed a portable digital microfluidic (DMF) system that allows for automated antibiotic susceptibility testing (AST) as well as bacterial classification (BC), measurements that can guide medical personnel on how best to treat a given patient's infection. The system features modules dedicated for integrated, parallel-scale absorbance and fluorescence measurements (Fig. 1A), a Bluetooth-enabled GPIO board that allows for seamless, wireless control over all of the integrated processes (Fig. 1B), a closed-loop heating and cooling system for long-term bacterial culture (Fig. 1C), and a DMF cartridge that allows monitoring bacterial growth (Fig. 1D). With its small footprint (15.9 cm × 25.9 cm), minimal power requirements, and intuitive, easy-to-use graphical interface (Fig. S5†), we propose that the system reported here represents a useful addition to the growing number of microfluidic systems that are being developed for miniaturized AST/BC.[17–35]

The work described here was inspired by the recent report of a DMF method used for AST,[39] which makes a strong case for how DMF may be useful for this type of application. As a next step relative to this first report, we sought to develop a fully integrated, sample-to-answer solution, which required critical innovations related to temperature/incubation and in-line sample analysis. We describe these innovations in detail below.

Integrated temperature control and incubation

The system reported here features a built-in heating unit[42] (Fig. S2†) that maintains the temperature of the bacterial culture system at 37 °C for the duration of the experiment. As shown in Fig. S11,† upon initiation, the temperature ramps up to reach 37 °C in around 5 min, and this temperature can be maintained at ±0.6 °C for over 24 h.

The key challenge in developing integrated heaters for DMF is countering the effects of droplet evaporation. Previous methods developed to address this challenge have typically relied on filling the device with oil or other immiscible media.[57–59] For example, the recently reported DMF-AST method[39] used devices filled with mineral oil, which provided excellent protection against evaporation, but the need to flood the device with oil adds another layer of complexity in the system and could potentially affect the oxygen transport. In the system reported here, an approach was adopted in which aqueous droplets were engulfed within a thin outer layer of oil,[60] an arrangement that facilitates efficient oxygen transport.[61] Vapor-lock (a low-viscosity, water-immiscible oil traditionally employed as a PCR encapsulation barrier) was used in the system. As shown in Fig. S12,† oil-encapsulation in vapor-lock resulted in substantial improvement, allowing for operation for up to 20 h at 37 °C with less than a 15% reduction to droplet volume from evaporative loss. As a final countermeasure for evaporation, relative droplet size was monitored in all experiments and was used as a correction factor in image processing in absorbance and fluorescence measurements, as described below.

Image analysis for real-time bacterial metabolic monitoring

The integrated system reported here features an on-board camera combined with an automated filter-slider and two banks of coloured LEDs to allow for hands-free switching between absorbance (Fig. S7A†) and fluorescence (Fig. S7B†) imaging modes. In the latter, the signal in the green (G) and blue (B) channels was suppressed, preserving high signal in the red (R) channel for fluorescent analysis of resorufin (λ_{ex}/λ_{em} = 560 nm/580 nm[62]) for AST and BC. After images were collected, a rigorous pre-processing regimen (including corrections for colour, distortion, perspective, and luminosity) was implemented (Fig. S6†), which transforms all images into time-stamped stacks of regions of interest (ROIs)

of each of the droplets being evaluated, prior to droplet contour detection and quantitative analysis.

We are aware of four previously reported fully integrated DMF systems relying on on-board image processing,[48,63–65] which have relied on specific lighting and contrast conditions to identify droplet contours for image analysis. In initial work, similar methods were tested here, but were found to be unreliable when propagated through the long incubation times required for the current application (16 h). Thus, a custom convolutional neural network (CNN) was developed (Fig. S8†) to allow for precise tracking of droplet shape and position for optical analysis. The CNN was trained with 495 ROI images (including those with augmentation to make the model insensitive to brightness changes and amount of blur), and the resulting network was validated on 135 ROI images, with high accuracy and low loss after 33 epochs (Fig. S9†). Image contours identified in ROIs in absorbance mode throughout the incubation period were then used to mask and normalize the signals in fluorescence mode ROIs to correct for the effects of minor evaporative losses. We are aware of only a single report of machine learning being used with DMF[66] (for a completely different application – segmenting images of adherent cells), and propose that the straightforward application of this technique to identify outlines of droplets may be a useful innovation for the community to use, going forward.

Assays for phenotypic AST and BC

Equipped with a fully integrated DMF system for bacterial culture and analysis, we turned to developing assays for phenotypic AST and BC. Three substrates (resazurin, RGP and

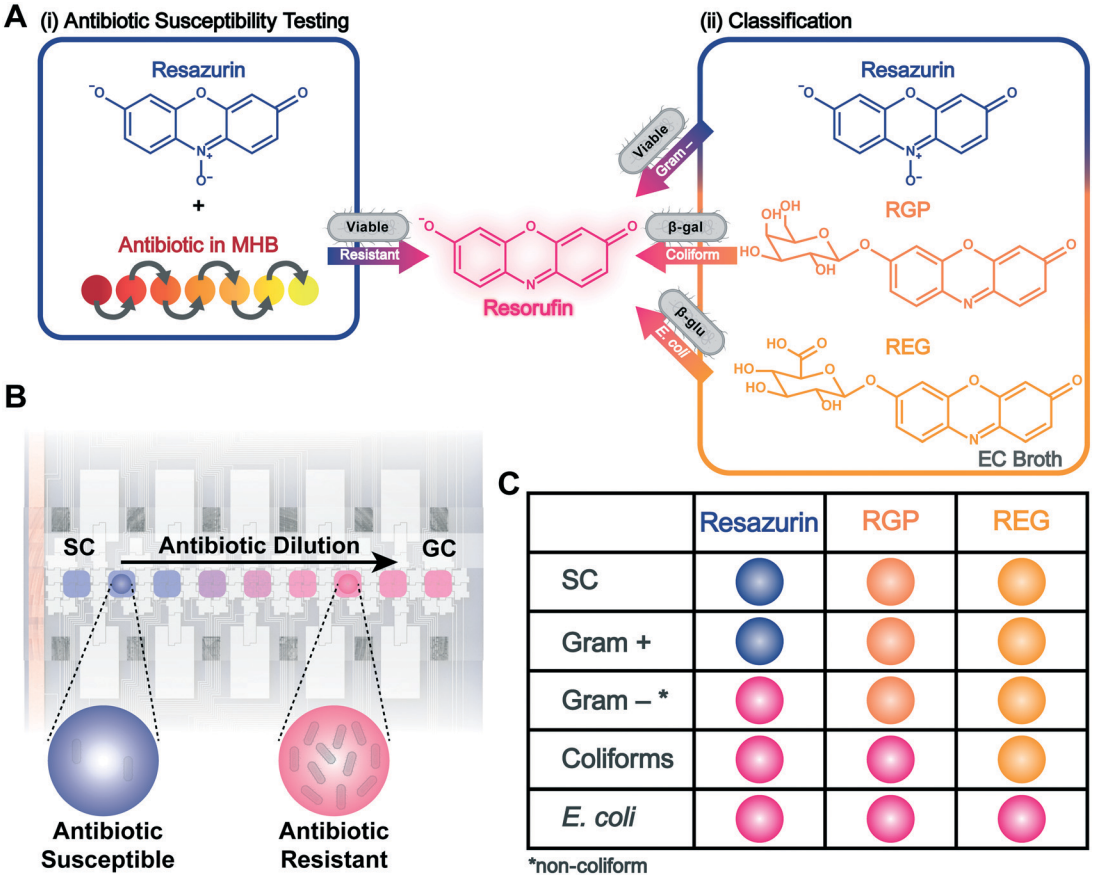

Fig. 2 Assays for automated AST and BC on DMF. (A) i. Cartoon illustrating how AST is performed with resazurin dye, which indicates bacterial cell metabolism (a marker of viability) upon conversion to the highly fluorescent product, resorufin. Resazurin is combined with seven serial dilutions of an antibiotic (gradient from red to yellow) in Mueller Hinton broth (MHB). ii. Cartoon illustrating how BC is performed, classifying bacteria based on their ability to convert the weakly fluorescent resazurin (indicating bacterial growth), resorufin beta-D-galactopyranoside (RGP) [indicating bacterial expression of beta-galactosidase (β-gal)], or resorufin beta-D-glucuronide (REG) [indicating bacterial expression of beta-glucuronidase (β-glu)] to resorufin in EC broth. (B) Cartoon illustrating nine droplets on a DMF device including the dilution series of antibiotic concentration as well as sterility and growth controls (SC and GC, respectively). Each droplet other than the SC is inoculated with a bacterial density of 5×10^5 CFU mL^{-1}, and the presence of the fluorescent product resorufin is used to identify concentrations of antibiotics to which bacteria are resistant (pink, viable), or susceptible (blue, non-viable). (C) Cartoon illustrating the expected combinations for three sample droplets used for BC (right columns) for various bacteria (left column). Each sample droplet contained either resazurin (blue), RGP (orange), or REG (light orange), which can be converted to resorufin (pink and fluorescent) for BC of the tested bacterial strains (5×10^5 CFU mL^{-1}). All experiments included a SC set (sample droplets with no bacteria).

REG) were employed to monitor the metabolic activity of 5×10^5 CFU mL^{-1} bacteria at 37 °C, to mimic standard broth microdilution methods,[53] based on their conversion to resorufin (Fig. 2A). Resazurin,[62] RGP[67] and REG[68] are weakly fluorescent, while resorufin exhibits strong fluorescence. Resorufin production was monitored *via* fluorescence imaging in 5–10 min intervals for at least 16 h in each experiment.

In AST experiments (Fig. 2A i), seven 2-fold antibiotic dilutions were performed on DMF in MHB, a non-specific culture broth used in standard broth microdilution assays,[53] containing resazurin. Equal volume droplets of bacterial suspensions were then added to the dilution series to monitor the effect of antibiotic concentrations on metabolism; bacteria resistant to an antibiotic at a specific concentration remained viable and reduced resazurin to resorufin, while susceptible bacteria did not.[22] An SC droplet without antibiotics and bacteria served as a negative control, and a GC droplet containing bacteria but no antibiotic served as a positive control (Fig. 2B). The time required for resorufin production was used to determine to the antibiotic concentrations to which bacteria were susceptible or resistant, to generate growth curves for MIC determination.

In BC experiments (Fig. 2A ii), tests were developed to probe for the presence of Gram-positive *vs.* Gram-negative bacteria, with viability indicated by conversion of resazurin to resorufin[22] in EC broth, which contains bile salts to prevent the growth of Gram-positive bacteria.[69] Among the latter, non-coliform *vs.* coliform bacteria classification was tested by conversion of RGP to resorufin as a result of characteristic beta-galactosidase (β-gal) expression in coliforms.[13,14,67] Among the latter, non-*E. coli vs. E. coli* was indicated by the conversion of REG to resorufin as a result of beta-glucuronidase (β-glu) expression, common in most *E. coli* strains.[68,70] These distinctions are important, as there are widely different treatments for Gram-positive *vs.* Gram-negative bacterial infections, while identifying the presence of coliforms is relevant in food and water quality testing.[13,14] In addition, *E. coli* is the leading cause of UTIs[11] and is one of the most common bacteria causing bloodborne infections.[71] In typical experiments, three replicate droplets of a bacterial sample were mixed with droplets containing resazurin, RGP, or REG, and were classified on the basis of the pattern of resorufin fluorescence after incubation for a suitable time (Fig. 2C).

AST to determine MIC on DMF

AST was performed on DMF with two model *E. coli* strains isolated from human urine, *E. coli* 1001728[12] and *E. coli* CFT073.[51] *E. coli* 1001728 is resistant to 33 antibiotics from various classes including penicillins, cephalosporins, carbapenems, quinolones and amino-glycosides and has reported susceptibility to nitrofurantoin and tigecycline.[72] Given that nitrofurantoin and ciprofloxacin (a quinolone) are common first-line UTI antibiotics[73,74] and that *E. coli* 1001728 is susceptible to the former and resistant to the latter,[72] these antibiotics were selected for AST to contrast different growth profiles. *E. coli* CFT073 is a common uropathogenic clonal line[75] and is susceptible to both ciprofloxacin[73] and nitrofurantoin, as confirmed here by standard broth microdilution methods (Tables S1 and S2†), serving as an antibiotic-susceptible strain.

During AST experiments, the production of the fluorescent product resorufin was monitored in droplets with seven antibiotic dilutions for up to 16 h on DMF *via* time-lapse imaging. Growing bacteria produced a sigmoidal fluorescent curve with respect to time, comprising four phases: a first phase of low steady signal, a second phase of rapid signal increase, a third phase of high steady signal (with duration that varied depending on the strain and growth conditions), and a fourth phase of declining signal (Fig. 3). The signals were normalized, and the time required for bacteria to reach the first mid-point of the curve, t_M, (found in phase 2) was recorded for each condition. In typical experiments, the GCs were among the first samples to show exponential signal increases (with the smallest t_M), followed by solutions containing increasing antibiotic concentrations.

Importantly, over the course of >40 experiments, no significant fluorescent signal increases were observed in SCs, confirming that the DMF devices were prepared and handled aseptically and that there was no observation of cross contamination among adjacent droplets. Pixel intensities of droplet images reached t_M within approximately 4–6 h at most antibiotic concentrations for both *E. coli* strains investigated, except for the droplets with the highest nitrofurantoin concentrations displaying bacterial growth, which took approximately 9–16 h (Fig. 3A and C). This lag in resorufin production for *E. coli* incubated with nitrofurantoin may be attributed to the time-dependant action of the drug, in contrast to ciprofloxacin, which is concentration-dependant.[74,76] Note that for clinical applications, the observation of low bacterial growth at antibiotic concentrations several dilutions away from the susceptible breakpoint value may not be as important as other effects; thus, in the future, a 4–6 h experiment may be sufficient to guide clinical decisions.

Resorufin fluorescence intensity has been widely used as an 'endpoint' marker for bacterial metabolic activity in AST and other applications.[22] Here, we chose instead to use a method similar to what was first reported by Mariscal *et al.*,[77] in which the time required to reach a particular fluorescence threshold (in this case, the mid-point of the sigmoidal curve, t_M) was used as a proxy for bacterial density. This strategy was first confirmed to be feasible in well-plates (as per Fig. S13,† the relationship between t_M and inoculation density is linear with $R^2 = 0.995$), and then was applied to the data acquired by DMF to generate viability curves relative to antibiotic concentration. Using the mid-point-time method allowed determination of viability 30 min to 4 hours earlier than the equivalent endpoint method.

Resorufin/midpoint data generated in the DMF system were compared against AST results generated from optical density measurements *via* standard broth microdilution in

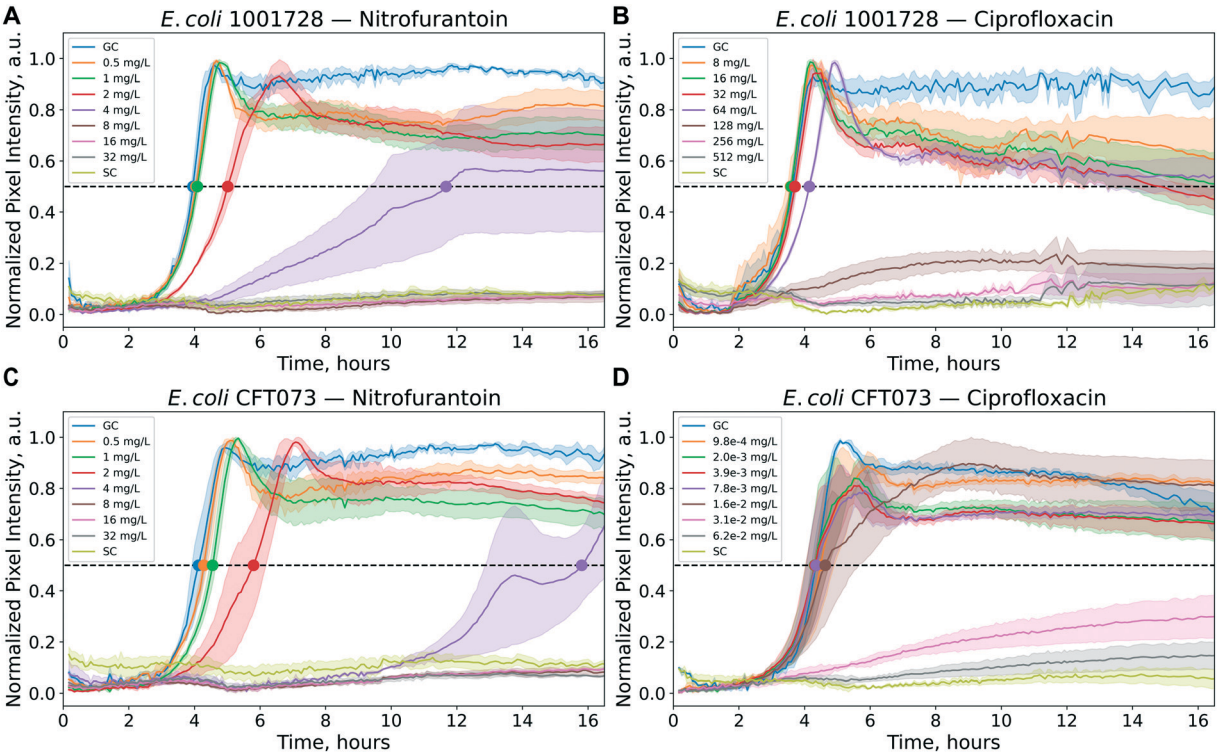

Fig. 3 Bacterial resorufin production curves in DMF AST experiments. Plots of normalized fluorescent signal as a function of time for droplets containing no antibiotic (GC, blue), increasing concentrations of antibiotic (orange, green, red, purple, brown, pink, grey), and no bacteria (SC, yellow). Shaded regions represent standard error of fluorescence measured in n = 3–4 replicate experiments, unless otherwise specified. Coloured dots indicate the average time t_M at which each signal from droplets with growing bacteria reached the mid-point of the curve (dashed black line). (A) *E. coli* 1001728 incubated with nitrofurantoin. (B) *E. coli* 1001728 incubated with ciprofloxacin. (C) *E. coli* CFT073 incubated with nitrofurantoin. (D) *E. coli* CFT073 incubated with ciprofloxacin.

well plates [the International Organization for Standardization (ISO) 20776-1 reference method[78]] for the same bacteria and antibiotics. As shown in Fig. 4, similar trends were observed when fitting the data obtained from the two methods using the Gompertz function.[27,79] Specifically, the DMF method (Fig. 4A and C) and the reference method (Table S1†) indicated the same MIC value for nitrofurantoin applied to both *E. coli* strains – 8 mg L^{-1} (this value is below the 32 mg mL^{-1} susceptibility breakpoint,[54] a result that, in a clinical setting, would recommend the drug for treatment). Likewise, the DMF method (Fig. 4B) and the reference method (Table S2†) indicated the same MIC value for ciprofloxacin applied to for *E. coli* 1001728 – 128 mg L^{-1} (this value is above the 4 mg mL^{-1} resistance breakpoint,[54] a result that, in a clinical setting, would recommend against use of the drug for treatment). Finally, the DMF method (Fig. 4D) and the reference method (Table S2†) indicated different MIC values for ciprofloxacin applied to for *E. coli* CFT073 – 0.031 mg L^{-1} (DMF) and 0.016 mg L^{-1} (reference test) (although different, both values are far below the 1 mg mL^{-1} susceptibility breakpoint,[54] meaning that both results, if acquired in a clinical setting, would correctly recommend the drug for treatment).

Most importantly, the MICs obtained by the DMF method for all of the conditions tested satisfy the ISO 20776-2 method[3] – that is, each value determined by DMF is in "essential agreement" with the values from the broth microdilution assays (*i.e.*, MICs from the developed method are within plus or minus one doubling dilution step from the MICs determined with the reference method). Likewise, the results of both the DMF method and the reference test used here are also in "category agreement" (*i.e.*, the susceptible, intermediate and resistance categorizations were the same *via* both methods). Finally, the close agreement between these very different methods suggests that there are minimal effects on bacterial growth from DMF manipulation, which is consistent with previous observations in DMF bacterial culture applications.[38]

BC on DMF

BC was performed and validated on DMF by culturing four species of bacteria that are known, among others, to cause UTIs (*E. coli*, *K. pneumoniae*, *P. mirabilis* and *S. aureus*)[11,80] after exposure to three different EC broths containing substrates resazurin, RGP or REG. Resorufin production in each droplet was monitored by fluorescence at 37 °C (Fig. 5 and S14†). Each sample droplet displayed a unique BC profile over time, related to the bacterial species. Maximum fluorescence was detected within 4–7.5 h of incubation in

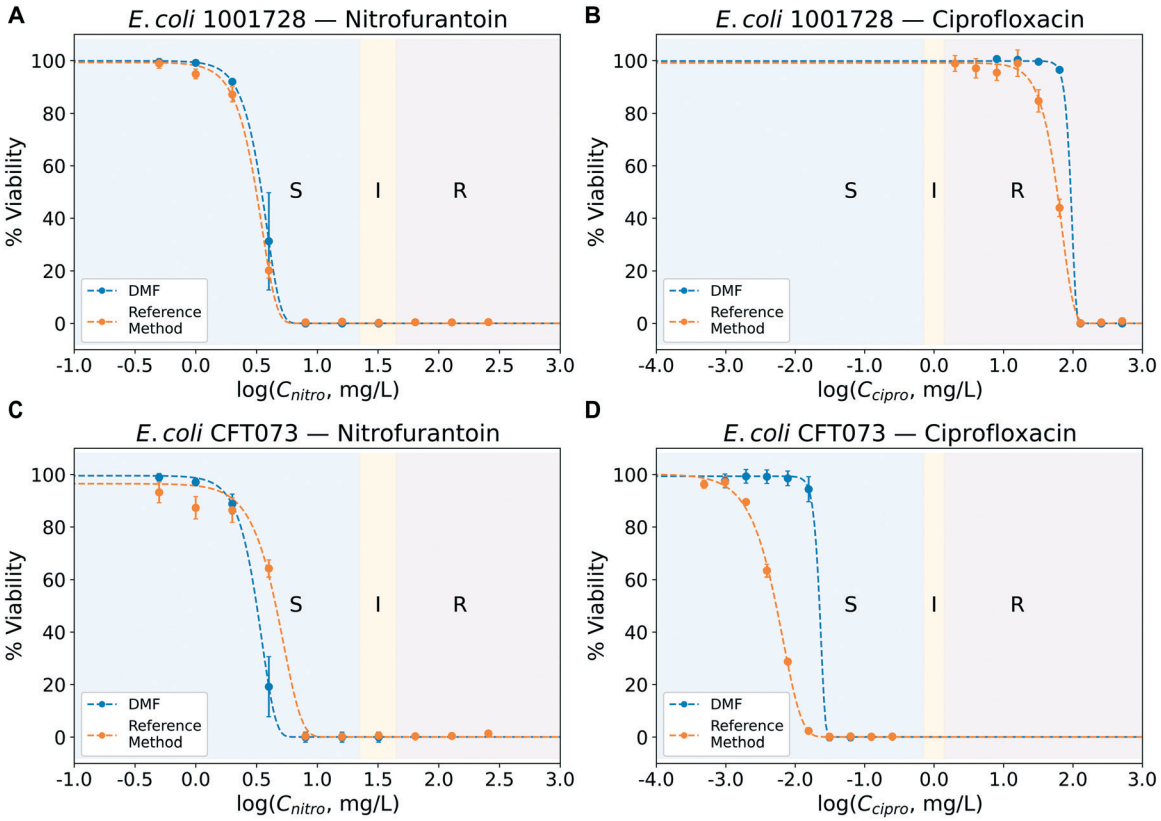

Fig. 4 Percent viability of bacteria at varied antibiotic concentrations (C_{nitro} and C_{cipro}) for DMF measurements (blue markers) compared to standard broth microdilution reference method (orange markers). Error bars represent standard error for n = 3–4 replicates per condition. Dashed lines represent a Gompertz function fitting[27,79] of bacterial viability. Antibiotic concentration ranges at which bacterial growth indicates susceptible (S-left), intermediate (I-middle) and resistant (R-right) classifications are represented in the respective coloured regions of the plots. (A) *E. coli* 1001728 incubated with nitrofurantoin. (B) *E. coli* 1001728 incubated with ciprofloxacin (C) *E. coli* CFT073 incubated with nitrofurantoin. (D) *E. coli* CFT073 incubated with ciprofloxacin. Note that the x axes are base-10 logarithm of antibiotic concentration in mg mL^{-1}. Thus (for example), axis values −1.0, 0.0, and +1.0 represent 0.1, 1.0, and 10 mg mL^{-1} antibiotic, respectively.

positive samples. A custom peak finding algorithm was developed to automatically detect the conversion of a substrate and classify the sample based on each marker. As predicted, *E. coli* converted all three substrates since it is a Gram-negative coliform that commonly expresses β-glu and β-gal, resulting in strong resorufin signals in all three droplets (Fig. 5A). *K. pneumoniae*, a Gram-negative coliform, metabolized both RGP and resazurin; no fluorescence signal was observed in REG droplets since *K. pneumoniae* does not express β-glu (Fig. 5B). *P. mirabilis*, a non-coliform Gram-negative bacterium, only reduced resazurin since it does not express either β-gal or β-glu (Fig. 5C). Finally, droplets with Gram-positive *S. aureus* had insignificant levels of resorufin production (no peak was identified), since bacterial growth was inhibited by the presence of bile salts in the EC broth.[69] In typical BC experiments, nine droplets were evaluated, allowing for simultaneous BC of two bacterial samples in parallel (in addition to controls). Depending on the need, future iterations with this system might feature higher sample throughput (including sample replicates) or additional BC assignments (with different markers or maker

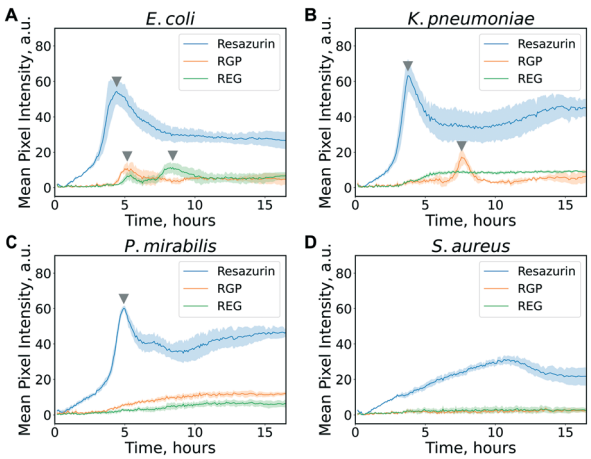

Fig. 5 DMF bacterial classification results. Plots of resorufin fluorescence as a function of time for replicate droplets of bacteria exposed to resazurin (blue), resorufin beta-D-galactopyranoside (RGP, orange) or beta-D-glucuronide (REG, green), in EC broth for (A) *E. coli* CFT073, (B) *K. pneumoniae*, (C) *P. mirabilis*, and (D) *S. aureus*. Shaded regions represent standard error of 3 replicates per condition and grey triangles indicate the maxima located using the peak finding algorithm.

combinations – for example, sodium azide to inhibit Gram-negative bacterial growth[81]).

Finally, an interesting 'halo' phenomenon was observed in droplets containing coliform bacteria in BC experiments, with brighter resorufin fluorescence at the edges of each droplet than in the centre (Fig. S14†). We attribute this phenomenon to gas production *via* lactose fermentation, which is expected in EC broth.[13,14] The gas that is produced appears to have an inhibitory effect on resorufin fluorescence, which is in equilibrium with its non-fluorescent analogue dihydroresorufin.[82] The equilibrium between the two analogues is affected by the presence of an oxidant (*e.g.*, O_2) or a reductant (*e.g.*, sugar). Specifically, in the DMF experiments, it seems that fluorescence is quenched near the centre of the droplet, while the edges of the droplet (exposed to the surrounding O_2) remains highly fluorescent. The halo effect was not observed to impact the peak-detection identification algorithm, but it might be useful additional information in the future, to differentiate between bacterial species that are otherwise similar but with different rates or mechanisms of lactose fermentation. Finally, this phenomenon might be fertile ground for probing with the recently reported DMF systems bearing spatially sensitive oxygen sensors.[39]

Simultaneous AST and BC on DMF

There are many impressive examples of conventional microfluidic systems[17–35] and DMF[39] that have been applied to bacterial AST and related applications. But while there are some commercial systems relying on non-microfluidic technology that allow for simultaneous phenotypic AST and BC, as far as we are aware, this has not been demonstrated on a microfluidic platform previously. With this in mind, we sought to determine whether the current system could be configured to carry this operation out, in two different modes: (i) AST (for MIC determination) combined with BC, and (ii) breakpoint testing (for susceptible, intermediate and resistant categorical results) of two antibiotics combined with BC.

According to the ISO 20776-2, the minimum number of consecutive 2-fold dilutions in an AST to determine a MIC is five.[3] With five antibiotic dilutions, as well as a GC and a SC, a total of seven droplets are required on the DMF device to perform AST for MIC determination. Since the maximum capacity of the DMF device used in this work is nine droplets, a method was developed to process five test droplets plus GC and SC droplets for AST and one test droplet and one SC droplet for a truncated BC assignment (*E. coli*-positive or -negative with REG) on a single device. In a series of DMF experiments, simultaneous ciprofloxacin AST and *E. coli* BC were performed for five bacterial strains (two *E. coli* strains, *K. pneumoniae*, *P. mirabilis* and *S. aureus*). As shown Table 1, all strains were correctly identified as *E. coli*-positive or -negative, and MICs were in category agreement (and essential agreement, when the exact MIC value was determined) with reference methods (Table S2†).

For applications in which a MIC determination is not required, a less exhaustive process can be used, known as breakpoint testing. In this type of assessment, bacterial samples were categorized (upon exposure to two threshold concentrations of antibiotic) as being susceptible, intermediate or resistant (S, I, R) to an antibiotic.[3] In these tests, two

Table 1 Results of simultaneous ciprofloxacin AST (with antibiotic concentrations based on the CLSI[54] to determine MIC values and categorize bacteria as susceptible/blue, intermediate/yellow, or resistant/pink) and *E. coli* classification on DMF for samples containing *E. coli* 1001728, *E. coli* CFT073, *K. pneumoniae* 700603, *S. aureus* 29213, or *P. mirabilis* 29906

Strain	*E. coli* BC		AST Ciprofloxacin							
				Susceptible		Intermediate	Resistant			MIC on DMF (mg/L)
	SC[a]	*E. coli*	GC[b]	0.25 mg/L	0.5 mg/L	1 mg/L	2 mg/L	4 mg/L	SC[a]	
E. coli 1001728	N	Y	+	+	+	+	+	+	–	≥ 8 Resistant
E. coli CFT073	N	Y	+	–	–	–	–	–	–	≤0.25 Susceptible
K. pneumoniae ATCC® 700603™	N	N	+	+	–	–	–	–	–	0.5 Susceptible
S. Aureus ATCC® 29213™	N	N	+	–	–	–	–	–	–	≤0.25 Susceptible
P. mirabilis ATCC® 29906™	N	N	+	–	–	–	–	–	–	≤0.25 Susceptible

[a] SC = sterility control. [b] GC = growth control, "Y" indicates peak detected for REG turnover in BC experiments, "N" indicates no peak detected for REG turnover in BC experiments, "+" indicates a sigmoidal curve with measurable mid-point time t_M in AST experiments and "–" indicates non-sigmoidal fluorescence profile (lacking a measurable mid-point time t_M) in AST experiments.

Table 2 Simultaneous ciprofloxacin and nitrofurantoin breakpoint testing (with antibiotic concentrations based on the CLSI[54] to categorize bacteria as susceptible/blue, intermediate/yellow, or resistant/pink), *E. coli* ID and coliform classification on DMF for samples containing *E. coli* 1001728

Strain	BC			Breakpoint Testing							
					Ciprofloxacin			Nitrofurantoin			
	SC[a]	Coliform	*E. coli*	GC[b]	1 mg/L	2 mg/L	SIR[c]	32 mg/L	64 mg/L	SIR[c]	SC[a]
E. coli 1001728	N	Y	Y	+	+	+	R	–	–	S	–

[a] SC = sterility control. [b] GC = growth control. [c] SIR = susceptible (S), intermediate (I), resistant (R) classification, "Y" indicates peak detected for REG (*E. coli*) or RGP (coliform) turnover in BC experiments, "N" indicates no peak detected for REG (*E. coli*) or RGP (coliform) turnover in BC experiments, "+" indicates a sigmoidal curve with measurable mid-point time t_M in breakpoint tests and "–" indicates non-sigmoidal fluorescence profile (lacking a measurable mid-point time t_M) in breakpoint tests.

droplets each were devoted to breakpoint testing (for ciprofloxacin and nitrofurantoin) and three for BC workup, including *E. coli* classification (using RGP), coliform classification (using REG) and a combined sterility control (containing both REG and RGP solutions). Multidrug resistant *E. coli* 1001728 was used to test this system as a proof-of-concept (Table 2 and Fig. S15†). Within 4 h, fluorescence intensity reached its half maximal value in the breakpoint test GC and in both ciprofloxacin droplets, allowing for correct classification of the strain as being ciprofloxacin resistant. Around the 6.5 h time point, conversion of RGP to resorufin was observed for coliform classification, and after 10.5 h, REG was converted to resorufin for *E. coli* classification. Finally, after 16 h there was no growth observed in the nitrofurantoin droplets, confirming susceptibility to this drug.

Conclusions

In this work, we reported a fully integrated and automated DMF platform for real-time AST and BC *via* monitoring the conversion of non-fluorescent metabolic markers to fluorescent products. A new instrument was purpose-built for this application that included an integrated heating module combined with oil-shell protection from evaporation, and a machine-learning-enabled imaging system designed for rapid droplet identification and analysis using a low-cost colour camera. Custom methods were developed using a single multipurpose device, permitting (for the first time in the microfluidics literature) combinations of assays including seven-point AST (with one antibiotic) of one sample, BC of two samples, simultaneous five-point AST (with one antibiotic) and BC of one sample, and multiplexed breakpoint testing (with multiple antibiotics) with BC of one sample. These methods are fully automated, such that there is no user intervention required after sample loading, and no requirement of ancillary equipment such as incubators or microscopes. Bacterial metabolic activity could be detected as early as 4–7.5 h by monitoring fluorescence intensity of the produced resorufin.

The method was validated by application to testing uropathogenic *E. coli* strains with UTI antibiotics ciprofloxacin and nitrofurantoin. BC was achieved simultaneously with ciprofloxacin AST for various types of bacteria that can cause UTIs: *E. coli*, *K. pneumoniae*, *P. mirabilis* and *S. aureus*. Finally, a proof-of-concept multiplexed system for breakpoint testing of two antibiotics, with *E. coli* and coliform BC was investigated. Automated, DMF-enabled classification of all bacterial strains was found to be correct, while results of DMF-enabled AST and breakpoint tests were all in category agreement and essential agreement, where applicable, with reference methods. These data demonstrate that the new all-in-one DMF system can be used to accurately monitor bacterial growth and phenotype, which could be expanded for use with other antibiotics, metabolic substrates and bacterial species that were not explored in this work. Further applications of the system for bacterial studies may include investigating polymicrobial populations, assessing synergistic effects of antibiotics and direct testing of clinical specimens.

Author contributions

C. R. N. and S. O. K. conceived of the idea for microfluidic evaluation of bacterial growth for AST and BC, and all bacterial growth and analysis experiments were carried out by C. R. N. in the S. O. K. lab. A. A. S designed, built, and validated DMF instrumentation, performed device fabrication and optimized image processing in the A. R. W. lab. A. A. S and C. R. N interpreted results and wrote the manuscript with assistance from all authors.

Conflicts of interest

There are no conflicts to declare.

Acknowledgements

This research was supported in part by the Canadian Institutes of Health Research (Foundation grant no. FDN-148415) and the Natural Sciences and Engineering Research

Council of Canada (Discovery grant no. RGPIN-2016-06090 and RGPIN 2019-04867). The research was also supported by the Society for Laboratory Automation and Screening (SLAS), under award number: SLASFG2019; any opinions, findings, and conclusions or recommendations expressed in this material are those of the authors and do not necessarily reflect those of SLAS. Figure components were created with BioRender.com. We thank Dr. Azza Al-Mahrouki (Centre for Pharm. Oncology, Univ. Toronto) for assistance with Cytation 5 multi-mode reader measurements. We thank Prof. Stefan Nagl and Qiu Wenting (Hong Kong Univ. Sci. Technol.), and Dr. Michael D. M. Dryden, Dr. Erica Y. Scott, Dr. Mark P. Pereira and Harrison S. Edwards (Univ. Toronto) for fruitful discussions. We thank Joshua Dahmer and Louise Dupoiron (Univ. Toronto) for technical support. AAS thanks the Centre for Research and Applications in Fluidic Technologies (CRAFT) for a graduate fellowship, and ARW thanks the Canada Research Chair (CRC) program for a CRC.

Notes and references

1 G. Maugeri, I. Lychko and R. Sobral, *et al.*, *Biotechnol. J.*, 2019, **14**, 1700750.
2 S. Sengupta, M. K. Chattopadhyay and H. P. Grossart, *Front. Microbiol.*, 2013, **4**, 47.
3 ISO, *Int. Stand. ISO 20776-22007*, 2007.
4 C. A. Petti, *Clin. Infect. Dis.*, 2007, **44**, 1108–1114.
5 P. E. Fournier, M. Drancourt and P. Colson, *et al.*, *Nat. Rev. Microbiol.*, 2013, **11**, 574–585.
6 S. J. Smith, C. R. Nemr and S. O. Kelley, *J. Am. Chem. Soc.*, 2017, **139**, 1020–1028.
7 N. G. Schoepp, T. S. Schlappi and M. S. Curtis, *et al.*, *Sci. Transl. Med.*, 2017, **9**, eaal3693.
8 P. A. C. Braga, A. Tata and V. Gonçalves dos Santos, *et al.*, *RSC Adv.*, 2013, **3**, 994–1008.
9 C. A. D. Burnham, J. Leeds and P. Nordmann, *et al.*, *Nat. Rev. Microbiol.*, 2017, **15**, 697–703.
10 S. Puttaswamy, S. K. Gupta and H. Regunath, *et al.*, *Arch. Clin. Microbiol.*, 2018, **9**, 83.
11 B. Foxman, *Nat. Rev. Urol.*, 2010, **7**, 653–660.
12 N. Gupta, B. M. Limbago and J. B. Patel, *et al.*, *Clin. Infect. Dis.*, 2011, **53**, 60–67.
13 Environmental Agency, *Drinking Water and Health*, National Academies Press, Washington, D.C., 1977.
14 P. Feng, W. D. Stephen and M. A. Grant, *et al.*, *Bacteriol. Anal. Man.*, 2002, **3**, 1–14.
15 H. Leonard, R. Colodner and S. Halachmi, *et al.*, *ACS Sens.*, 2018, **3**, 2202–2217.
16 J. H. H. Jorgensen and M. J. J. Ferraro, *Clin. Infect. Dis.*, 2009, **49**, 1749–1755.
17 D. B. Weibel, W. R. DiLuzio and G. M. Whitesides, *Nat. Rev. Microbiol.*, 2007, **5**, 209–218.
18 Z. A. Khan, M. F. Siddiqui and S. Park, *Biotechnol. Lett.*, 2019, **41**, 221–230.
19 J. Q. Boedicker, L. Li and T. R. Kline, *et al.*, *Lab Chip*, 2008, **8**, 1265–1272.
20 R. Mohan, A. Mukherjee and S. E. Sevgen, *et al.*, *Biosens. Bioelectron.*, 2013, **49**, 118–125.
21 J. Choi, J. Yoo and M. Lee, *et al.*, *Sci. Transl. Med.*, 2014, **6**, 267ra174.
22 J. D. Besant, E. H. Sargent and S. O. Kelley, *Lab Chip*, 2015, **15**, 2799–2807.
23 L. D. Renner, J. Zan and L. I. Hu, *et al.*, *Appl. Environ. Microbiol.*, 2017, **83**, e02449-16.
24 T. J. Abram, H. Cherukury and C. Y. Ou, *et al.*, *Lab Chip*, 2020, **20**, 477–489.
25 Y. T. Kao, T. S. Kaminski and W. Postek, *et al.*, *Lab Chip*, 2020, **20**, 54–63.
26 D. C. Spencer, T. F. Paton and K. T. Mulroney, *et al.*, *Nat. Commun.*, 2020, **11**, 5328.
27 O. Scheler, K. Makuch and P. R. Debski, *et al.*, *Sci. Rep.*, 2020, **10**, 1–8.
28 I. Michael, D. Kim and O. Gulenko, *et al.*, *Nat. Biomed. Eng.*, 2020, **4**, 591–600.
29 R. Wille, B. Li and R. Drechsler, *et al.*, in *Lecture Notes in Electrical Engineering*, Springer, 2020, vol. 611, pp. 71–87.
30 A. V. Nguyen, M. Azizi and M. Yaghoobi, *et al.*, *Anal. Chem.*, 2021, **93**, 5789–5796.
31 Ö. Baltekin, A. Boucharin and E. Tano, *et al.*, *Proc. Natl. Acad. Sci.*, 2017, **114**, 9170–9175.
32 W. Bin Lee, C. Y. Fu and W. H. Chang, *et al.*, *Biosens. Bioelectron.*, 2017, **87**, 669–678.
33 M. Veses-Garcia, H. Antypas and S. Löffler, *et al.*, *Front. Microbiol.*, 2018, **9**, 1530.
34 W. Kang, S. Sarkar and Z. S. Lin, *et al.*, *Anal. Chem.*, 2019, **91**, 6242–6249.
35 C. R. Nemr, S. J. Smith and W. Liu, *et al.*, *Anal. Chem.*, 2019, **91**, 2847–2853.
36 A. H. C. Ng, M. Lee and K. Choi, *et al.*, *Clin. Chem.*, 2015, **61**, 420–429.
37 I. Barbulovic-Nad, H. Yang and P. S. Park, *et al.*, *Lab Chip*, 2008, **8**, 519–526.
38 S. H. Au, S. C. C. Shih and A. R. Wheeler, *Biomed. Microdevices*, 2011, **13**, 41–50.
39 W. Qiu and S. Nagl, *ACS Sens.*, 2021, **6**, 1147–1156.
40 D. G. Rackus, M. D. M. Dryden and J. Lamanna, *et al.*, *Lab Chip*, 2015, **15**, 3776–3784.
41 C. Dixon, A. H. C. Ng and R. Fobel, *et al.*, *Lab Chip*, 2016, **16**, 4560–4568.
42 T. Narahari, J. Dahmer and A. A. Sklavounos, *et al.*, *Manuscript in Preparation*, 2021.
43 R. Fobel, C. Fobel and A. R. Wheeler, *Appl. Phys. Lett.*, 2013, **102**, 193513.
44 I. Swyer, R. Fobel and A. R. Wheeler, *Langmuir*, 2019, **35**, 5342–5352.
45 PyQT, *PyQt Reference Guide*, 2012.
46 G. Bradski, *Dr. Dobb's Journal of Software Tools*, 2000.
47 P. Ge, X. Ling and J. Wang, *et al.*, in *Proceedings of the 2019 IEEE Global Communications Conference (GLOBECOM)*, 2019, pp. 1–6.
48 A. A. Sklavounos, J. Lamanna and D. Modi, *Clin. Chem.*, 2021, DOI: 10.1093/clinchem/hvab180, in press.

49 O. Ronneberger, P. Fischer and T. Brox, in *Lecture Notes in Computer Science*, 2015, vol. 9351, pp. 234–241.
50 D. P. Kingma and J. Ba, 2014, arXiv:1412.6980.
51 H. L. Mobley, D. M. Green and A. L. Trifillis, *et al.*, *Infect. Immun.*, 1990, **58**, 1281–1289.
52 M. D. M. Dryden, D. D. G. Rackus and M. H. Shamsi, *et al.*, *Anal. Chem.*, 2013, **85**, 8809–8816.
53 I. Wiegand, K. Hilpert and R. E. W. Hancock, *Nat. Protoc.*, 2008, **3**, 163–175.
54 Clinical and Laboratory Standards Institute, *M100-S25 Performance Standards for Antimicrobial Susceptibility Testing; 25th Informational Supplement*, 2015.
55 Because of uneven illumination; droplets near the edges of the device had lower signal than droplets in the center of the device. We accommodated this difference by positioning the GC droplet (which is expected to have the highest signal) in the 'darkest' position. The GC's maximum signal was then used as a threshold for normalization as described in step 6 of the image processing procedure.
56 P. Virtanen, R. Gommers and T. E. Oliphant, *et al.*, *Nat. Methods*, 2020, **17**, 261–272.
57 S. Kalsi, S. Sellars and C. Turner, *et al.*, *Micromachines*, 2017, **8**, 111.
58 S. Kalsi, M. Valiadi and C. Turner, *et al.*, *Lab Chip*, 2019, **19**, 168–177.
59 S. Kalsi, M. Valiadi and M. N. Tsaloglou, *et al.*, *Lab Chip*, 2015, **15**, 3065–3075.
60 A. M. Foudeh, D. Brassard and M. Tabrizian, *et al.*, *Lab Chip*, 2015, **15**, 1609–1618.
61 J. Zhai, H. Li and A. H. H. Wong, *et al.*, *Microsyst. Nanoeng.*, 2020, **6**, 6.
62 G. G. Guilbault and D. N. Kramer, *Anal. Chem.*, 1965, **37**, 1219–1221.
63 P. Q. N. Vo, M. C. Husser and F. Ahmadi, *et al.*, *Lab Chip*, 2017, **17**, 3437–3446.
64 L. M. Y. Leclerc, G. Soffer and D. H. Kwan, *et al.*, *Biomicrofluidics*, 2019, **13**, 034106.
65 S. Anderson, B. Hadwen and C. Brown, *Lab Chip*, 2021, **21**, 962–975.
66 J. Lamanna, E. Y. Scott and H. S. Edwards, *et al.*, *Nat. Commun.*, 2020, **11**, 5632.
67 J. Hofmann and M. Sernetz, *Anal. Chim. Acta*, 1984, **163**, 67–72.
68 G. Magro, R. E. S. Bain and C. A. Woodall, *et al.*, *Environ. Sci. Technol.*, 2014, **48**, 9624–9631.
69 M. Begley, C. G. M. Gahan and C. Hill, *FEMS Microbiol. Rev.*, 2005, **29**, 625–651.
70 M. Manafi, W. Kneifel and S. Bascomb, *Microbiol. Rev.*, 1991, **55**, 335–348.
71 D. J. Biedenbach, G. J. Moet and R. N. Jones, *Diagn. Microbiol. Infect. Dis.*, 2004, **50**, 59–69.
72 *ATCC® NDM-1 Strains*, https://www.atcc.org/~/media/PDFs/MarketingMaterial/Microbiology/NDM-1Strains.ashx, (accessed 24 February 2021).
73 A. Chockalingam, S. Stewart and L. Xu, *et al.*, *Antibiotics*, 2019, **8**, 170.
74 M. N. Toosky, J. T. Grunwald and D. Pala, *et al.*, *J. Med. Microbiol.*, 2020, **69**, 52–62.
75 J. S. Kao, D. M. Stucker and J. W. Warren, *et al.*, *Infect. Immun.*, 1997, **65**, 2812–2820.
76 F. Fransen, M. J. B. Melchers and J. Meletiadis, *et al.*, *J. Antimicrob. Chemother.*, 2016, **71**, 2883–2889.
77 A. Mariscal, R. M. Lopez-Gigosos and M. Carnero-Varo, *et al.*, *Appl. Microbiol. Biotechnol.*, 2009, **82**, 773–783.
78 ISO, *Int. Stand. ISO 20776-12006*, 2019.
79 R. J. W. Lambert and J. Pearson, *J. Appl. Microbiol.*, 2000, **88**, 784–790.
80 A. L. Flores-Mireles, J. N. Walker and M. Caparon, *et al.*, *Nat. Rev. Microbiol.*, 2015, **13**, 269–284.
81 M. L. Snyder and H. C. Lichstein, *J. Infect. Dis.*, 1940, **67**, 113–115.
82 J. O'Brien, I. Wilson and T. Orton, *et al.*, *Eur. J. Biochem.*, 2000, **267**, 5421–5426.